Sensibility Analysis of the Virtual Synchronous Generator Using a Small-Signal Model

Julio Hernández-Ramírez, Hany Nassim

***Abstract*—The application of voltage source converters (VSCs) to integrate renewable energies into the power electrical systems has reached higher levels, leading to a displacement of synchronous generation and the weakening of the networks. Novel approaches have been proposed in the last decade to mimic the operation of the synchronous machines (SMs) trying to reproduce the electromagnetic and electromechanic dynamics throughout power electronics, giving robustness to the power system and inertial support. To understand the impact of the so-called grid-forming operation of VSCs, this paper assesses the control approach known as the virtual synchronous generator. The stability of the steady state is studied throughout the eigenvalues of the linear state-space model in the synchronous framework DQ. By developing parametric variations, the impact of control gains is checked, and the stability is verified using extensive time-domain simulations carried out in PSCAD/EMTDC.**

***Keywords*—Grid-forming converters, virtual synchronous generators, stability analysis, small-signal.**

I. Introduction

THE environmental concerns in the world have impulse the massive integration of environment friendly energies into the electrical networks. Eventually, this has also led to a progressive reduction of carbon-based generation produced using SMs [1], [2]. The new-generation technologies rely on the extensive utilization of inverter based resources (IBRs) and VSCs, bringing new opportunities to operate the system more efficiently, flexibly, and controllable [3], [4]. However, these new technologies are also changing the traditional operative paradigms of power systems because IBRs are faster than SMs, and their dynamical behavior is predominantly dictated by the implemented control strategies. This has given the birth of instability issues in the system, wideband oscillatory interactions, subsynchronous oscillations, the reduction of inertia in the networks, and diminishing of the short circuit ratio (SCR) among others [5]. To maintain the correct operation of the electrical network, it is essential to have the presence of SMs in the system that can form the system, providing enough support to establish the voltage magnitude and the frequency of the system. These are features that the VSCs could not provide some decades ago because, in those days, the main goal of IBRs was to integrate renewable energies into the system, but looking for the maximum extraction of power. This operative paradigm was known as grid-following, where the VSCs were seen as a current-controlled source that attained the synchronization by a phase-locked loop (PLL) [6], [7].

Formely, the inverters have used the PLL to attain the successfully synchronization to the grid, this control element can also provide a way to filter disturbances. The study of its behavior has been done following linear and nonlinear analysis, bifurcation theory, phase diagram and other tools. Some issues that synchronization using PLLs have are: In weak grids, where synchronous generation is poor, the voltage and frequency stability is deficient, this also difficults the correct operation of power converters. During large disturbances in the grid, it is hard for the PLL tracking the phase and frequency of the system. This can lead to oscillations that degrade the performance of the converter. In severe cases, the synchronization can be loss. The information of phase and frequency is highly sensitive to the impedance of the grid; hence, larger impedances can affect the stability margins of the PLL, increasing the risk of instability. The risk of interactions increases due to the inner and outer loop controls depend on voltage and current, and these variables also impact in the information of phase that the PLL tries to track.

As an alternative to raise the capabilities of the VSCs, newer control strategies have been developed to endow these devices with the ability to behave as a SM [8]. Following this approach, the VSCs are seen as voltage-controlled sources, and the operation is known as grid-forming. Grid-forming VSCs offer some outstanding features, such as the ability to maintain the voltage in a system with very low SMs, the capability to operate in systems with small SCRs, and provide inertial support to the system, as well as damping to oscillations in the system [9].

Typical approaches to control VSCs as grid-forming are the power synchronization control, the droop control, the synchronverter, the virtual oscillator, and the virtual synchronous generator (VSG); several of these methods are focused on reproducing the dynamics of the swing equation of SMs [7], [10]. These approaches are widely studied to understand the stability features that grid-forming VSCs offer; this has been done using small-signal and large-signal analysis. Large-signal analysis is mainly based on time-domain simulations to assess the performance of the system under large disturbances using electromagnetic transient (EMT), or root mean square (RMS) simulations. On the other hand, linear analysis carries out the study using time and frequency domains to develop models, either as state space or impedance

This work was supported by Siemens Energy. Julio Hernández-Ramírez is with Siemens Energy, S. de R.L. de C.V Mexico, Portfolio Consulting PR (e-mail of corresponding author: julio.hernandez@siemens-energy.com). Hany Nassim is with Siemens Energy Inc USA, Grid Analysis & Planning (e-mail: hany.nassim@siemens-energy.com).

Paper submitted to the International Conference on Power Systems Transients (IPST2025) in Guadalajara, Mexico, June 8-12, 2025.

models. These approaches have permitted a comprehensive understanding of phenomena, such as oscillatory interactions, harmonic coupling, control design, sensitivity analyses, and bifurcations, among others.

This contribution presents a stability analysis of the VSG, checking the impact of the control parameters on the system's performance. The study uses a linear state-space model to identify the change in the eigenvalues when parametric changes are done, and the dynamical behavior is confirmed using nonlinear time-domain electromagnetic simulations. The content of this work is organized as follows: section II presents the test case, and the dynamical model is given as a set of ordinary differential equations (ODEs). The model is based on an average model, and the performance of the ODEs is validated using PSCAD/EMT, where the model is simulated using detailed pulse width modulation (PWM) and power electronics models. In section III, the stability of the steady state is studied using eigenvalue traces to determine the effect of parametric variations on the stability. Finally, the conclusions are provided.

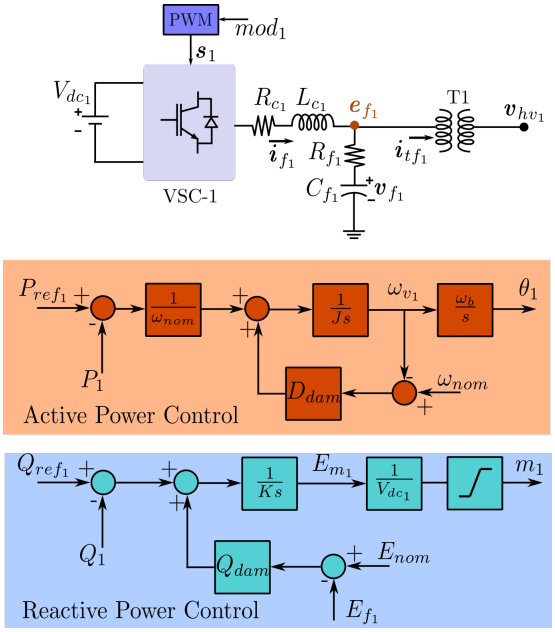

Fig. 1. Control strategy of the VSG.

II. Modelling of the Test System

A. Clarifications

This paper uses bold symbols to denote three-phase variables in the reference framework DQ (voltage or currents), so writing $\boldsymbol{i}$ is the current $\boldsymbol{i} = \begin{bmatrix} i_D & i_Q \end{bmatrix}^T$. To change from ABC to DQ the Park transform is used:

$$\boldsymbol{T}(\theta) = \frac{2}{3}\begin{bmatrix} \cos(\theta) & \cos\left(\theta - \frac{2\pi}{3}\right) & \cos\left(\theta + \frac{2\pi}{3}\right) \\ -\sin(\theta) & -\sin\left(\theta - \frac{2\pi}{3}\right) & -\sin\left(\theta + \frac{2\pi}{3}\right) \\ \frac{1}{2} & \frac{1}{2} & \frac{1}{2} \end{bmatrix} \tag{1}$$

with $\theta = \omega_b t$, being ω_b the base angular frequency of the system. Lowercase fonts are used to define time-domain variables, and uppercase fonts denote the steady-state value of any variable. The argument (t) is omitted in the equations for brevity. All the equations presented in this work are written in per unit (p.u.). The VSCs are considered typical two-level power converters that operate using sinusoidal PWM, and the systems under study are assumed to be balanced.

B. Virtual synchronous generator

The objective of the VSG is to ensure that the VSCs can participate in the inertial support of the grid, automatically changing the active and reactive power dispatch according to the frequency and voltage amplitude of the system. The control is based on [11], [12], and the block diagram control is given in Fig. 1. Two control loops are used; one regulates the active power of the VSC, while a second loop supports the voltage of the system, controlling the reactive power.

Both loops try to reproduce the dynamic behavior of a synchronous generator. The synchronization of the VSC is attained following a similar approach as the swing equation. It is noted that both control loops add a damping feature that helps to reduce the effect of oscillations in the system. On the other hand, the VSC has an LC filter that is interconnected to the grid through a step-up transformer. The dynamical equations of the control are the following:

$$\begin{aligned} \frac{d\theta_1}{dt} &= \omega_b \omega_{v_1} \\ \frac{d\omega_{v_1}}{dt} &= \frac{1}{J}\left[\frac{P_{ref_1} - P_1}{\omega_{nom}} + D_{dam}(\omega_{nom} - \omega_{v_1})\right] \\ \frac{dE_{m_1}}{dt} &= \frac{1}{K}\left[Q_{ref_1} - Q_1 + Q_{dam}(E_{nom} - E_{f_1})\right] \end{aligned} \tag{2}$$

P_1 and Q_1 are the active and reactive power that are measured using the current in terminals of the VSC ($\boldsymbol{i}_{f_1}$), and the voltage in the filter ($\boldsymbol{e}_{f_1}$). P_{ref_1} and Q_{ref_1} are the control references of the powers, ω_{nom} is the nominal angular frequency of the system in p.u., E_{nom} is the reference of voltage magnitude in p.u., E_{f_1} is the voltage magnitude in p.u. of e_{f_1}. Finally, ω_b is the base angular frequency of the system. The outcomes from these control loops are the angle θ_1, and the magnitude m_1, of the modulation signals:

$$mod_1 = m_1 \begin{bmatrix} \cos(\theta_1) \\ \cos\left(\theta_1 - \frac{2\pi}{3}\right) \\ \cos\left(\theta_1 + \frac{2\pi}{3}\right) \end{bmatrix} \tag{3}$$

Using each modulation signal, the PWM is built by comparing the corresponding modulation against a sawtooth waveform of higher frequency, and then commutation patterns, s_a, s_b, and s_c are created. Finally, we have the PWM patterns [13]:

$$\boldsymbol{s}_1 = \begin{bmatrix} s_a - \frac{1}{3}(s_a + s_b + s_c) \\ s_b - \frac{1}{3}(s_a + s_b + s_c) \\ s_c - \frac{1}{3}(s_a + s_b + s_c) \end{bmatrix} \tag{4}$$

The following six equations complement the dynamical model of the VSC:

$$\frac{d}{dt}\begin{bmatrix}\boldsymbol{i}_{f_1}\\ \boldsymbol{v}_{f_1}\\ \boldsymbol{i}_{tf_1}\end{bmatrix} = \begin{bmatrix}\frac{\omega_b}{L_{c_1}}(2V_{dc_1}\boldsymbol{T}(\theta)\boldsymbol{s}_1 - R_{f_1}\boldsymbol{i}_{f_1} - \boldsymbol{e}_{f_1} - L_{c_1}\boldsymbol{P}\boldsymbol{i}_{f_1})\\ \frac{\omega_b}{C_{f_1}}(\boldsymbol{i}_{f_1} - \boldsymbol{i}_{tf_1} - C_{f_1}\boldsymbol{P}\boldsymbol{v}_{f_1})\\ \frac{\omega_b}{L_{tf_1}}(\boldsymbol{e}_{f_1} - \boldsymbol{v}_{hv_1} - L_{tf_1}\boldsymbol{P}\boldsymbol{i}_{tf_1})\end{bmatrix} \tag{5}$$

The transformer is modeled as an ideal transformer with a leakage inductance L_{tf_1}, whose high-voltage signal is represented by $\boldsymbol{v}_{hv_1}$. This signal would be different depending on the point where the VSC will be connected. The matrix $\boldsymbol{P}$ is included to model the cross-coupling between variables in D-axis and in Q-axis:

$$\boldsymbol{P} = \begin{bmatrix}0 & -1\\ 1 & 0\end{bmatrix} \tag{6}$$

It is worth mentioning that if the average model is used, then the PWM patterns in (4) are not used. Instead, they should be modeled as $mod_1/2$.

C. Nine bus system model

This work used the well-known nine-bus system, initially presented in [14]. However, in this case, two synchronous generators are replaced using VSG, and the third generator is changed to represent an equivalent electrical network. The system is given in Fig. 2, showing the currents and the voltage in each transmission line. A lumped-parameter PI circuit represents each transmission line, and the system's load models are modeled as constant impedance loads. Each VSG is modeled as the system given in Fig. 1. So, the model of the grid is the following 32 ODEs:

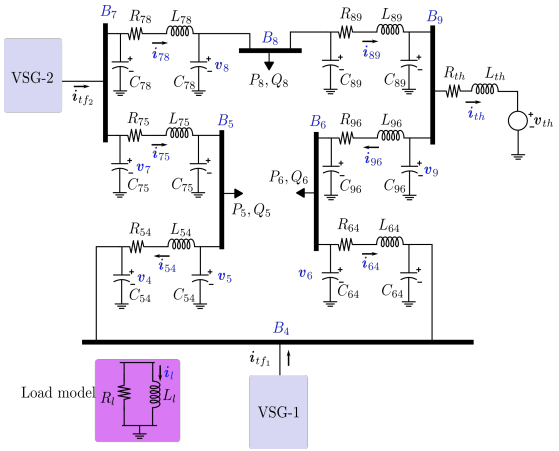

Fig. 2. Power system with penetration of VSG.

$$\frac{d}{dt}\begin{bmatrix}\boldsymbol{i}_{78}\\ \boldsymbol{v}_7\\ \boldsymbol{v}_8\\ \boldsymbol{i}_{89}\\ \boldsymbol{v}_9\\ \boldsymbol{i}_{75}\\ \boldsymbol{v}_5\\ \boldsymbol{i}_{96}\\ \boldsymbol{v}_6\\ \boldsymbol{i}_{54}\\ \boldsymbol{v}_4\\ \boldsymbol{i}_{64}\\ \boldsymbol{i}_{l_5}\\ \boldsymbol{i}_{l_8}\\ \boldsymbol{i}_{l_6}\\ \boldsymbol{i}_{th}\end{bmatrix} = \begin{bmatrix}\frac{\omega_b}{L_{78}}(\boldsymbol{v}_7 - R_{78}\boldsymbol{i}_{78} - \boldsymbol{v}_8 - L_{78}\boldsymbol{P}\boldsymbol{i}_{78})\\ \frac{\omega_b}{C_7}(\boldsymbol{i}_{tf_2} - \boldsymbol{i}_{78} - \boldsymbol{i}_{75} - C_7\boldsymbol{P}\boldsymbol{v}_7)\\ \frac{\omega_b}{C_8}(\boldsymbol{i}_{78} - \boldsymbol{i}_{89} - \boldsymbol{i}_{l_8} - \boldsymbol{v}_8/R_{l_8} - C_8\boldsymbol{P}\boldsymbol{v}_8)\\ \frac{\omega_b}{L_{89}}(\boldsymbol{v}_8 - R_{89}\boldsymbol{i}_{89} - \boldsymbol{v}_9 - L_{89}\boldsymbol{P}\boldsymbol{i}_{89})\\ \frac{\omega_b}{C_9}(\boldsymbol{i}_{89} - \boldsymbol{i}_{th} - \boldsymbol{i}_{96} - C_9\boldsymbol{P}\boldsymbol{v}_9)\\ \frac{\omega_b}{L_{75}}(\boldsymbol{v}_7 - R_{75}\boldsymbol{i}_{75} - \boldsymbol{v}_5 - L_{75}\boldsymbol{P}\boldsymbol{i}_{75})\\ \frac{\omega_b}{C_5}(\boldsymbol{i}_{75} - \boldsymbol{i}_{54} - \boldsymbol{i}_{l_5} - \boldsymbol{v}_5/R_{l_5} - C_5\boldsymbol{P}\boldsymbol{v}_5)\\ \frac{\omega_b}{L_{96}}(\boldsymbol{v}_9 - R_{96}\boldsymbol{i}_{96} - \boldsymbol{v}_6 - L_{96}\boldsymbol{P}\boldsymbol{i}_{96})\\ \frac{\omega_b}{C_6}(\boldsymbol{i}_{96} - \boldsymbol{i}_{64} - \boldsymbol{i}_{l_6} - \boldsymbol{v}_6/R_{l_6} - C_6\boldsymbol{P}\boldsymbol{v}_6)\\ \frac{\omega_b}{L_{54}}(\boldsymbol{v}_5 - R_{54}\boldsymbol{i}_{54} - \boldsymbol{v}_4 - L_{54}\boldsymbol{P}\boldsymbol{i}_{54})\\ \frac{\omega_b}{C_4}(\boldsymbol{i}_{54} + \boldsymbol{i}_{64} + \boldsymbol{i}_{tf_1} - C_4\boldsymbol{P}\boldsymbol{v}_4)\\ \frac{\omega_b}{L_{64}}(\boldsymbol{v}_6 - R_{64}\boldsymbol{i}_{64} - \boldsymbol{v}_4 - L_{64}\boldsymbol{P}\boldsymbol{i}_{64})\\ \frac{\omega_b}{L_{l_5}}(\boldsymbol{v}_5 - L_{l_5}\boldsymbol{P}\boldsymbol{i}_{l_5})\\ \frac{\omega_b}{L_{l_8}}(\boldsymbol{v}_8 - L_{l_8}\boldsymbol{P}\boldsymbol{i}_{l_8})\\ \frac{\omega_b}{L_{l_6}}(\boldsymbol{v}_6 - L_{l_6}\boldsymbol{P}\boldsymbol{i}_{l_6})\\ \frac{\omega_b}{L_{th}}(\boldsymbol{v}_9 - R_{th}\boldsymbol{i}_{th} - \boldsymbol{T}(\theta)\boldsymbol{v}_{th} - L_{th}\boldsymbol{P}\boldsymbol{i}_{th})\end{bmatrix}$$

$$\begin{aligned}C_7 &= C_{78} + C_{75}\\ C_8 &= C_{78} + C_{89}\\ C_9 &= C_{89} + C_{96}\\ C_5 &= C_{75} + C_{54}\\ C_6 &= C_{96} + C_{64}\\ C_4 &= C_{54} + C_{64}\end{aligned} \tag{7}$$

D. Validation of the dynamical system

For each VSG, a set of ODEs similar to (2)-(5) is obtained, and together to (7) the whole dynamical system is written. Table I gives the system's high-voltage side parameters. The impedances of the loads correspond to the following powers: $P_8 + jQ_8 = 100 + j35$ MVAR, $P_5 + jQ_5 = 125 + j50$ MVAR, and $P_6 + jQ_6 = 90 + j30$ MVAR. The parameters of each VSG are provided in Table II and Table III (the base values are provided for the electrical parameters, whereas the base values for the active power and reactive power control gains are 7.036×10^{-4} MVA$\cdot s^2$ and 6.12 kA respectively). Finally, the commutation frequency is 2.7 kHz in both VSC.

The transformers are connection Y-Y, with a ratio of 20 kV / 345 kV; the leakage inductance of $L_{tf_1} = 0.0576$ p.u., $L_{tf_2} = 0.0625$ p.u. (using $S_b = 100$ MVA) . The voltage in the equivalent grid is a balanced three-phase source with $v_{th_a} = 1.03\cos(\omega_0 t + 0.133)$ p.u.

To validate the performance of the ODEs, the system is numerically integrated (using zero initial conditions in all state variables) and simulated in PSCAD/EMTDC (the state variables start from zero, the simulation is carried out using a time-step of 1 μs, without ramping in the controls). The waveforms of some state variables are compared in Fig. 3 and Fig. 4. The comparison is done during the energization transient of the system, as well as in a steady state. Fig. 3 shows the currents in terminals of each VSC; it is noted that the model in PSCAD/EMTDC has a commutation ripple, while the ODEs only retain the information of the fundamental component of the dynamics. During the transient, it is harder

TABLE I
DATA OF THE GRID (345 KV, 100 MVA, 60 HZ)

Parameter	Value	Parameter	Value
R_{78}	0.0085 p.u.	L_{78}	0.072 p.u.
C_{78}	0.0745 p.u.	R_{89}	0.0119 p.u.
L_{89}	0.1008 p.u.	C_{89}	0.1045 p.u.
R_{75}	0.032 p.u.	L_{75}	0.161 p.u.
C_{75}	0.153 p.u.	R_{96}	0.039
L_{96}	0.17 p.u.	C_{96}	0.179 p.u.
R_{54}	0.01 p.u.	L_{54}	0.085 p.u.
C_{54}	0.088 p.u.	R_{64}	0.017 p.u.
L_{64}	0.092 p.u.	C_{64}	0.079 p.u.
R_{th}	0.001 p.u.	L_{th}	0.089 p.u.
R_{l_5}	0.8 p.u.	L_{l_5}	2 p.u.
R_{l_8}	1 p.u.	L_{l_8}	2.8571 p.u.
R_{l_6}	1.111 p.u.	L_{l_6}	3.333 p.u.

TABLE II
DATA OF THE VSG-1 (20 KV, 100 MVA, 60 HZ)

Parameter	Value	Parameter	Value
V_{dc_1}	1.4 p.u.	R_{c_1}	0.00157 p.u.
L_{c_1}	0.1947 p.u.	R_{f_1}	0.3099 p.u.
C_{f_1}	0.03041 p.u.	P_{ref_1}	1 p.u.
J	0.5625 p.u.	D_{dam}	49.398 p.u.
K	0.3825 p.u.	Q_{dam}	5.766 p.u.
Q_{ref_1}	0 p.u.	E_{f_1}	1.015 p.u.

TABLE III
DATA OF THE VSG-2 (20 KV, 100 MVA, 60 HZ)

Parameter	Value	Parameter	Value
V_{dc_1}	1.4 p.u.	R_{c_1}	0.00157 p.u.
L_{c_1}	0.1947 p.u.	R_{f_1}	0.3099 p.u.
C_{f_1}	0.03041 p.u.	P_{ref_1}	0.9 p.u.
J	0.5625 p.u.	D_{dam}	49.398 p.u.
K	0.3825 p.u.	Q_{dam}	5.766 p.u.
Q_{ref_1}	0 p.u.	E_{f_1}	1.02 p.u.

to appreciate this ripple; however, as is shown in Fig. 3-(b), in a steady state, the effect of the PWM is more visible.

On the other hand, Fig. 4 shows the response of the voltage in the bus B_5, and the current throughout the transmission line that goes from B_5 to B_4. These state variables have less harmonic content because the responses between the average and commutated models (PSCAD/EMTDC) almost overlap.

Again, this figure validates the energization transient and steady-state response. Other state variables of the model were also compared, and a good similarity was found between the ODEs and PSCAD, but they are not shown here for brevity. Once this task is completed, the dynamical model is validated, and we can trust that the model's performance in PSCAD can be studied using the ODEs instead of developing time-domain simulations.

III. STABILITY ANALYSIS

As seen from Fig. 3 and Fig. 4, the system is stable because the variables are bounded and do not diverge; this behavior can also be verified by computing the eigenvalues of the linear model in DQ. This reference framework has the advantage of mapping periodic orbits to a steady-state operating point. Then, around the invariant equilibrium point $(\boldsymbol{X}_{ss}, \boldsymbol{U}_{ss})$, the

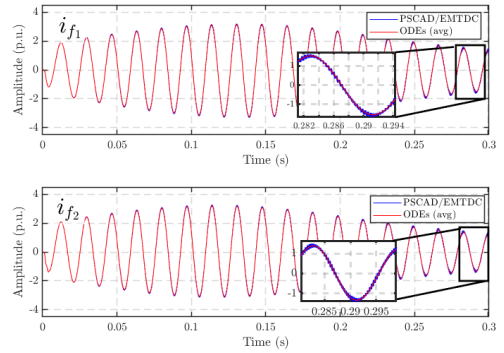

(a) Transient state

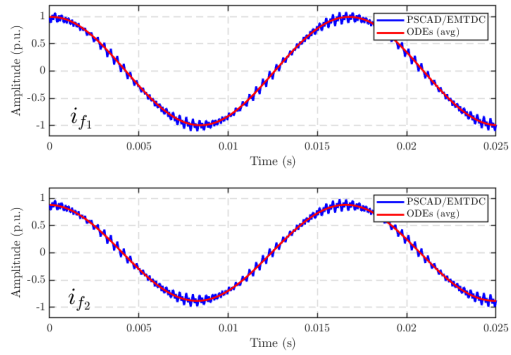

(b) Steady state

Fig. 3. Dynamical response of currents in terminals of each VSC.

dynamics of the large-signal model can be approximated by the small-signal model [15]:

$$\frac{d\Delta \boldsymbol{x}}{dt} = \left(\frac{\partial \boldsymbol{f}}{\partial \boldsymbol{x}} \bigg|_{\boldsymbol{X}_{ss}, \boldsymbol{U}_{ss}} \right) \Delta \boldsymbol{x} + \left(\frac{\partial \boldsymbol{f}}{\partial \boldsymbol{u}} \bigg|_{\boldsymbol{X}_{ss}, \boldsymbol{U}_{ss}} \right) \Delta \boldsymbol{u} \quad (8)$$

The eigenvalues for the system operating with the nominal parameters are given in Fig. 5; all are located on the left-hand side of the complex plane; therefore, the system should be stable, and this matches with the simulations done in PSCAD/EMTDC.

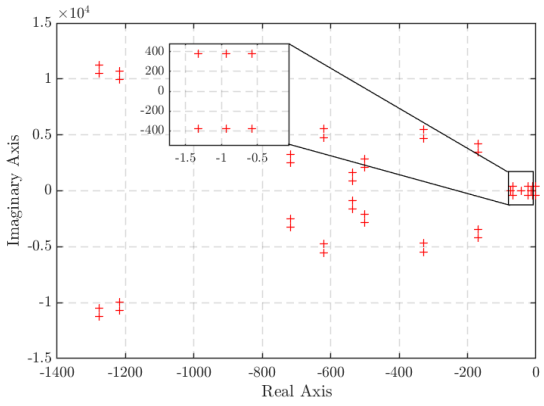

Fig. 5. Eigenvalues of the system in the nominal condition.

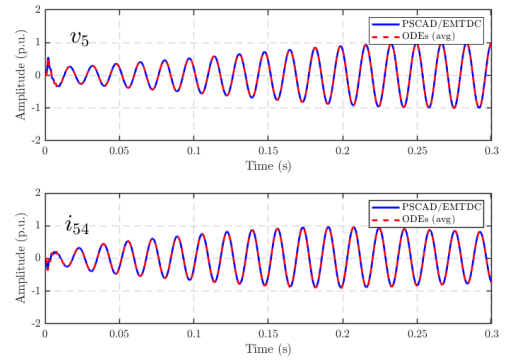

(a) Transient state

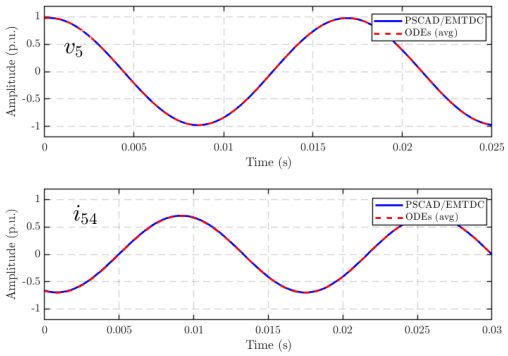

(b) Steady state

Fig. 4. Dynamical response of variables in the transmission network.

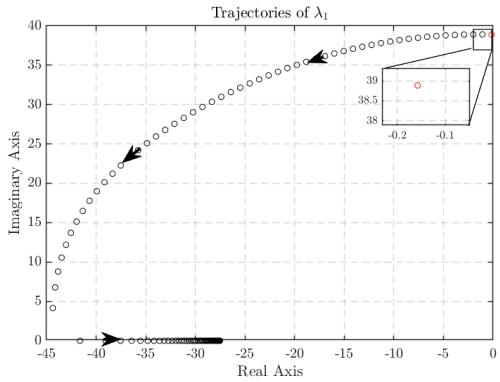

(a) Effect in the eigenvalue λ_1

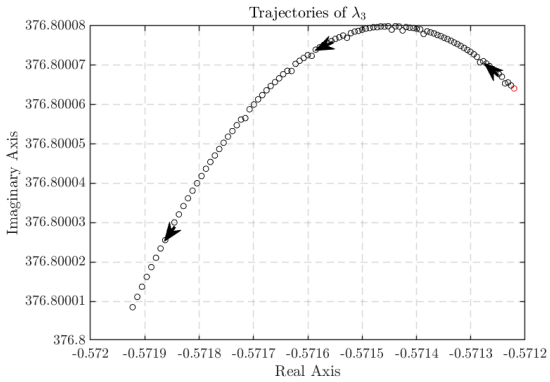

(b) Effect in the eigenvalue λ_3

Fig. 6. Impact of changes in $D_{dam} \in \left[10^{-6}, \quad 10^{2}\right]$ in VSG-1.

The dominant eigenvalues of the system are $\lambda_{1,2} = -0.5175 \pm j376.8$ and $\lambda_{3,4} = -0.937 \pm j376.478$. They have damping factors of $\xi_{1,2} = 0.001516$ and $\xi_{3,4} = 0.00249$, although the system is stable, it is poorly damped, so it can be prone to turn unstable. The system's stability is strongly influenced by several factors: the operating condition, the topology of the network, the load consumption, and the control gains, among others. The linear model is suitable to study the effect of parametric changes and small changes in the operating conditions around the steady state. Hence, some sensitivities are done to check the impact of parametric variations of the controls on the system's performance.

In the following subsections, the traces of the most dominant eigenvalues of the system are assessed.

A. Effect of the active power control: VSG-1

The effect of variations in the damping gain, D_{dam}, is presented in Fig. 6. The arrows point out the direction of the movement in the eigenvalues as D_{dam} increases from 10^{-6} to 100. It is worth mentioning that here, we only present the nearest eigenvalues to the imaginary axis (in the complex plane, this is $s = 0$); these eigenvalues are the interest because they can move toward the complex right-half plane.

The analysis indicates that the system remains stable despite the gain being almost zero; however, it has a very low damping ratio. When $D_{dam} = 1 \times 10^{-6}$ the system has dominant modes $\lambda_{1,2} = -0.1577 \pm j38.886$, with a frequency of 6.188 Hz. On the other hand, the impact of variations in J is illustrated in Fig. 7 (arrows indicate the direction of movement when J decreases); this parameter provokes the system to lose stability when $J \leq 0.088$, and a pair of modes with a frequency of 375.2 rad/s appears.

Time-domain simulations around the steady state are done to test the results above. To disturb the dynamics from the equilibrium point, a reference change in P_{set_2} from 0.9 p.u. to 0.85 p.u. and then returning to 0.9 p.u. is assessed. Fig. 8 shows the active power of both VSG diminishing the value of D_{dam} in VSG-1. It is seen that damped oscillations are presented, and the frequency of the oscillations is identified with the fast Fourier transform (FFT) with a value of 6.21 Hz.

Whereas in Fig. 9, the effect of J is assessed, it is validated that a value of $J = 0.088$ causes unstable oscillations in the system, and the FFT gives the oscillation frequency as 59.5 Hz. These results match those obtained with the small-signal analysis.

B. Effect of the active power control: VSG-2

It is found that gains $J \leq 0.0412$ cause instability in the system, with modes $\lambda_{1,2} = 0.0042 \pm j375$ (see Fig. 10-(b)); regarding the constant, D_{damp}, in Fig. 10-(a) it is appreciated that diminishing this value the system reduces the damping but remains stable. These outcomes are very similar to those of the VSG-1 and give insights into the dominant impact of the inertial constant on the stability; hence, the system is more susceptible to changes in J.

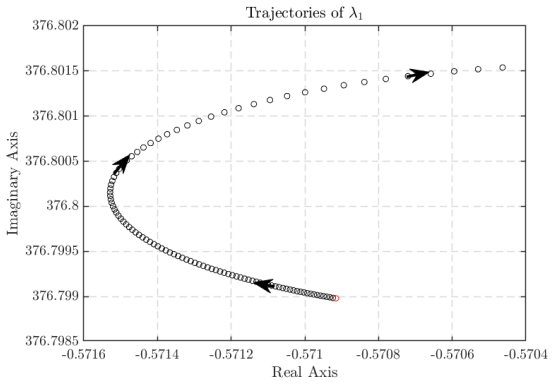

(a) Effect in the eigenvalue λ_1

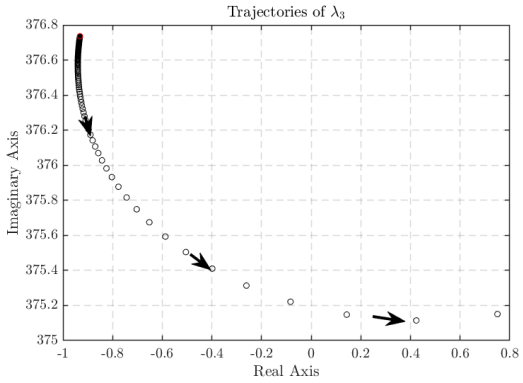

(b) Effect in the eigenvalue λ_3

Fig. 7. Impact of changes in $J \in \begin{bmatrix} 1.5, & 0.05 \end{bmatrix}$ in VSG-1.

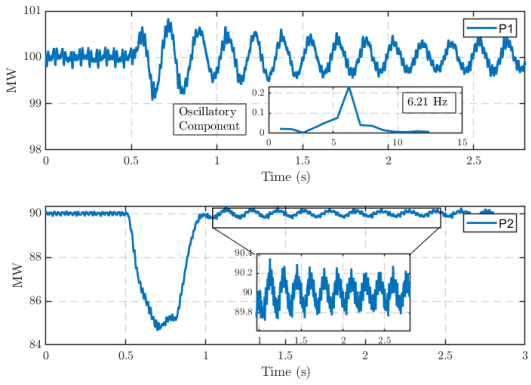

Fig. 8. Dynamical response when $D_{dam} = 1 \times 10^{-6}$.

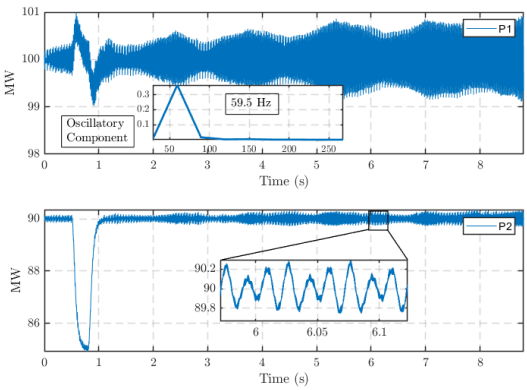

Fig. 9. Dynamical response when $J = 0.088$.

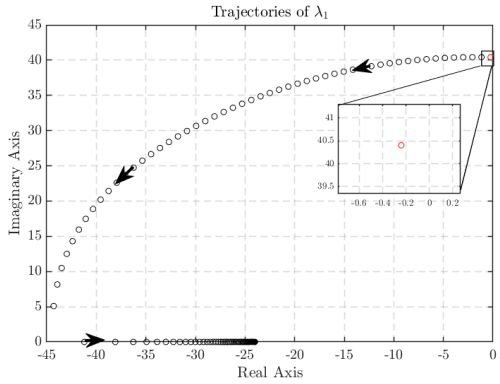

(a) Effect of variations in $D_{dam} \in \begin{bmatrix} 10^{-6}, & 100 \end{bmatrix}$

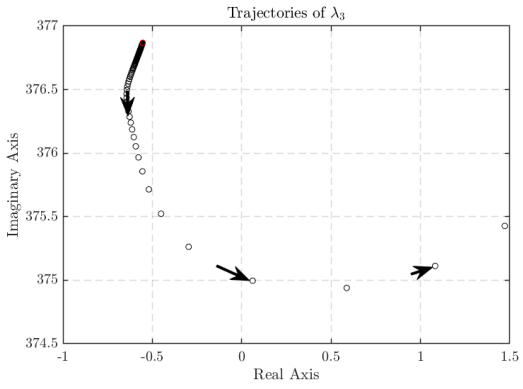

(b) Effect of variations in $J \in \begin{bmatrix} 1, & 0.01 \end{bmatrix}$

Fig. 10. Impact of changes in J and D_{dam} in VSG-2.

C. Effect of the reactive power control: VSG-1

The movement of λ_3 while varying the gain K in the range $\begin{bmatrix} 1 & 0.1 \end{bmatrix}$ is presented in Fig. 11-(b), showing that the system is unstable when $K \leq 0.161$ and detonating oscillations with a frequency of 376.2 rad/s. On the other hand, Fig. 11-(a) shows the traces of λ_1 when Q_{dam} changes in the range $\begin{bmatrix} 10 & 1 \times 10^{-3} \end{bmatrix}$, the system is less sensitive to this gain, because the dominant eigenvalues do not move far from the original location. Time-domain simulations given in Fig. 12 and Fig. 13 validates this behavior.

D. Effect of the reactive power control: VSG-2

The sensitivity results for this control are very similar to those of VSG-1. The traces of the eigenvalues are given in Fig. 14-(a) showing the sensitivity of the VSG-2 to changes in K, and Fig. 14-(b) depicts those results related to changes in Q_{dam}. Analyzing these results, it was found that the system is stable for $K \geq 0.1437$, because in Fig. 14-(a) is seen a movement to the right-hand side of complex plane. On the other hand, the traces showed in Fig. 14-(b) indicates the system would be stable although the Q_{dam} gain is changed because the most dominant eigenvalue does not move very

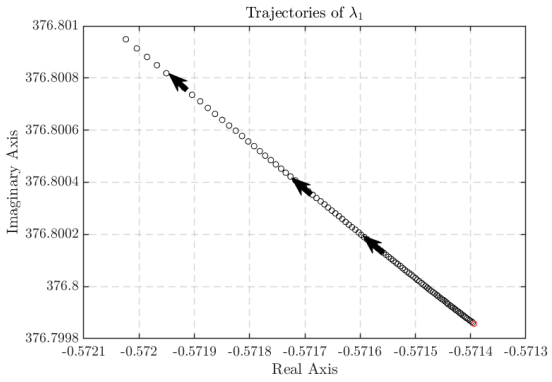

(a) Effect of variations in $Q_{dam} \in [10, \quad 1 \times 10^{-3}]$

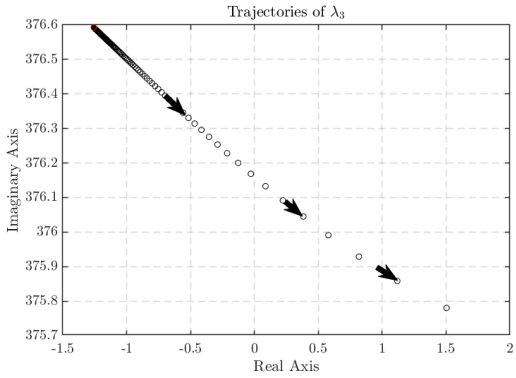

(b) Effect of variations in $K \in [1, \quad 0.1]$

Fig. 11. Impact of changes in K and Q_{dam} in VSG-1.

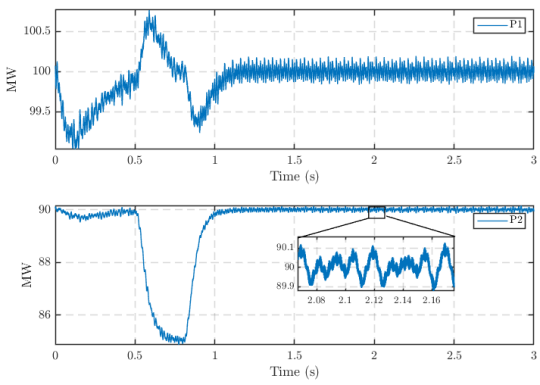

Fig. 12. Dynamical response when $Q_{dam} = 1 \times 10^{-3}$.

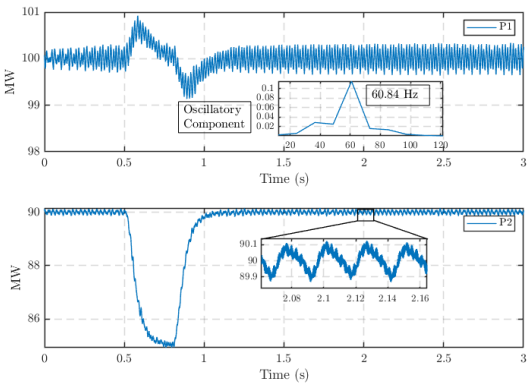

Fig. 13. Dynamical response when K=0.161.

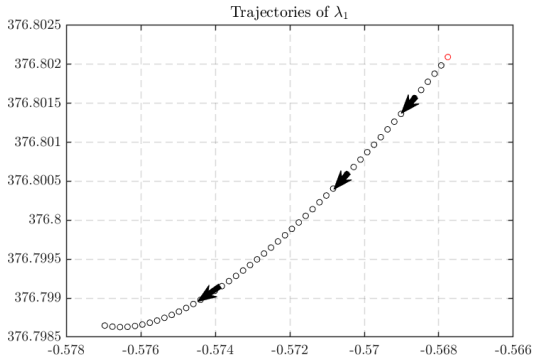

(a) Effect of variations in $Q_{dam} \in [10, \quad 1 \times 10^{-3}]$

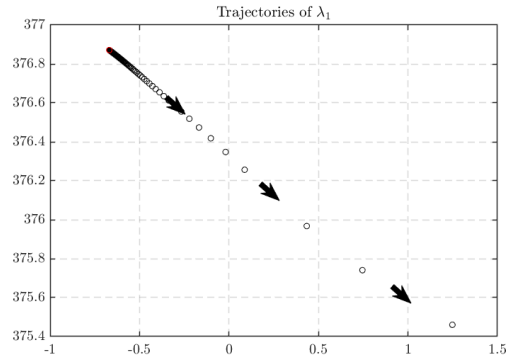

(b) Effect of variations in $K \in [1, \quad 0.1]$

Fig. 14. Impact of changes in K and Q_{dam} in VSG-2.

much from the initial position.

IV. Conclusions

This paper presented a small-signal analysis of the VSG control of VSCs based on linear state-space models. The analysis used an extensive eigenvalue location study to see the sensitivity of the modes of the system to parametric variation. It was tested the effects of the active and reactive power loop gains in the dynamical performance, finding that low-frequency oscillations can be presented. The validation of the dynamical model was done using PSCAD/EMTDC using a commutated model, where the PWM was modeled. The results showed a good match between the ODEs and the PSCAD simulation. Moreover, the results given by the small-signal analysis were verified using the large-signal model, indicating a match respecting the theoretical analyses.

V. Acknowledgment

The authors gratefully acknowledge Siemens Energy's contributions to financial support.

References

[1] A. U. Rehman, Z. Wadud, R. M. Elavarasan, G. Hafeez, I. Khan, Z. Shafiq, and H. H. Alhelou, "An optimal power usage scheduling

in smart grid integrated with renewable energy sources for energy management," *IEEE Access*, vol. 9, pp. 84 619–84 638, 2021.

[2] J. Luo, W. Zhuo, S. Liu, and B. Xu, "The optimization of carbon emission prediction in low carbon energy economy under big data," *IEEE Access*, vol. 12, pp. 14 690–14 702, 2024.

[3] Z. Tang, Y. Yang, and F. Blaabjerg, "Power electronics: The enabling technology for renewable energy integration," *CSEE Journal of Power and Energy Systems*, vol. 8, no. 1, pp. 39–52, 2022.

[4] G. S. Chawda, A. G. Shaik, O. P. Mahela, S. Padmanaban, and J. B. Holm-Nielsen, "Comprehensive review of distributed facts control algorithms for power quality enhancement in utility grid with renewable energy penetration," *IEEE Access*, vol. 8, pp. 107 614–107 634, 2020.

[5] N. Hatziargyriou, J. Milanovic, C. Rahmann, V. Ajjarapu, C. Canizares, I. Erlich, D. Hill, I. Hiskens, I. Kamwa, B. Pal, P. Pourbeik, J. Sanchez-Gasca, A. Stankovic, T. Van Cutsem, V. Vittal, and C. Vournas, "Definition and classification of power system stability – revisited & extended," *IEEE Transactions on Power Systems*, vol. 36, no. 4, pp. 3271–3281, 2021.

[6] Y. Wu, H. Wu, F. Zhao, Z. Li, and X. Wang, "Influence of pll on stability of interconnected grid-forming and grid-following converters," *IEEE Transactions on Power Electronics*, vol. 39, no. 10, pp. 11 980–11 985, 2024.

[7] X. Wang, M. G. Taul, H. Wu, Y. Liao, F. Blaabjerg, and L. Harnefors, "Grid-synchronization stability of converter-based resources—an overview," *IEEE Open Journal of Industry Applications*, vol. 1, pp. 115–134, 2020.

[8] R. H. Lasseter, Z. Chen, and D. Pattabiraman, "Grid-forming inverters: A critical asset for the power grid," *IEEE Journal of Emerging and Selected Topics in Power Electronics*, vol. 8, no. 2, pp. 925–935, 2020.

[9] R. Rosso, X. Wang, M. Liserre, X. Lu, and S. Engelken, "Grid-forming converters: Control approaches, grid-synchronization, and future trends—a review," *IEEE Open Journal of Industry Applications*, vol. 2, pp. 93–109, 2021.

[10] M. Tozak, S. Taskin, I. Sengor, and B. P. Hayes, "Modeling and control of grid forming converters: A systematic review," *IEEE Access*, vol. 12, pp. 107 818–107 843, 2024.

[11] H. Wu, X. Ruan, D. Yang, X. Chen, W. Zhao, Z. Lv, and Q.-C. Zhong, "Small-signal modeling and parameters design for virtual synchronous generators," *IEEE Transactions on Industrial Electronics*, vol. 63, no. 7, pp. 4292–4303, 2016.

[12] W. Wu, L. Zhou, Y. Chen, A. Luo, Y. Dong, X. Zhou, Q. Xu, L. Yang, and J. M. Guerrero, "Sequence-impedance-based stability comparison between vsgs and traditional grid-connected inverters," *IEEE Transactions on Power Electronics*, vol. 34, no. 1, pp. 46–52, 2019.

[13] S. Bacha, I. Munteanu, and A. Bratcu, *Power Electronic Converters Modeling and Control: with Case Studies*, ser. Advanced Textbooks in Control and Signal Processing. Springer London, 2013. [Online]. Available: https://books.google.com.mx/books?id=ijW3BAAAQBAJ

[14] P. M. Anderson and A. A. Fouad, *Power System Stability*, 2003, pp. 2–12.

[15] A. H. Nayfeh and B. Balachandran, *Applied Nonlinear Dynamics: Analytical, Computational and Experimental Methods (Wiley Series in Nonlinear Science)*. New York, NY, USA: Wiley, 2008.